

A *Spitzer*/IRAC Characterization of Galactic AGB and RSG Stars

Megan Reiter¹, Massimo Marengo², Joseph L. Hora³, and Giovanni G. Fazio³

¹ *Steward Observatory, University of Arizona, Tucson, AZ 85721, USA*

² *Department of Physics and Astronomy, Iowa State University, Ames, IA 50011, USA*

³ *Harvard-Smithsonian Center for Astrophysics, 60 Garden St. Cambridge, MA 02138-1516, USA*

Accepted 2014 Jul ??; Received 2014 Jul ??; in original form 2014 Jul ??

ABSTRACT

We present new *Spitzer*/IRAC observations of 55 dusty Long Period Variables (LPVs, 48 AGB and 6 RSG stars) in the Galaxy that have different chemistry, variability type, and mass-loss rate. O-rich AGB stars (including intrinsic S-type) tend to have redder $[3.6] - [8.0]$ colors than carbon stars for a given $[3.6] - [4.5]$ color due to silicate features increasing the flux in the $8.0\ \mu\text{m}$ IRAC band. For colors including the $5.8\ \mu\text{m}$ band, carbon stars separate into two distinct sequences, likely due to a variable photospheric C_3 feature that is only visible in relatively unobscured, low mass-loss rate sources. Semiregular variables tend to have smaller IR excess in $[3.6] - [8.0]$ color than Miras, consistent with the hypothesis that semiregular variables lose mass discontinuously. Miras have redder colors for longer periods while semiregular variables do not. Galactic AGB stars follow the period-luminosity sequences found for the Magellanic Clouds. Mira variables fall along the fundamental pulsation sequence, while semiregular variables are mostly on overtone sequences. We also derive a relationship between mass-loss rate and $[3.6] - [8.0]$ color. The fits are similar in shape to those found by other authors for AGBs in the LMC, but discrepant in overall normalization, likely due to different assumptions in the models used to derive mass-loss rates. We find that IR colors are not unique discriminators of chemical type, suggesting caution when using color selection techniques to infer the chemical composition of AGB dust returned to the ISM.

Key words: stars: AGB and post-AGB, carbon, mass loss – infrared: stars

1 INTRODUCTION

The Asymptotic Giant Branch (AGB) is the last evolutionary phase of low and intermediate mass stars ($M < 8\ M_\odot$), before the brief post-AGB phase that leads them to become white dwarfs. AGB stars are characterised by complex nucleosynthesis, high mass-loss rates, and variability. They are the source of a large fraction of the mass returned by stars to the Interstellar Medium (ISM, Sedlmayr 1994). In particular, they are believed to be the primary ‘dust factories’ in galaxies (Gehrz 1989; Boyer et al. 2012), even though recent observations have re-evaluated the role played by supernovae (see e.g. Matsuura et al. 2011; Dwek & Cherchneff 2011). It is clear, however, that understanding mass-loss in AGB stars is instrumental for modeling the chemical evolution of galaxies.

The composition of the material returned from AGB stars to the ISM depends on the chemistry of the star, which is determined by its initial mass and evolutionary history. The latter is crucially regulated by mass loss. Most stars enter the AGB with an intrinsic C/O abundance ratio less than

one (O-rich). In stars of $\sim 1.5 - 4\ M_\odot$ (Straniero et al. 1995, 1997) however, several dredge-up events following thermal pulses may drive the C/O ratio above unity. These stars become the so-called carbon stars. In stars above $\sim 4\ M_\odot$, however, carbon is destroyed by nuclear burning at the base of the convective envelope (Hot Bottom Burning; Smith & Lambert 1985; Boothroyd & Sackmann 1992) preventing it from reaching the surface of the star where it could be observed. These stars never transition to the carbon star phase. Mass limits constraining the formation of carbon stars depend on metallicity; low metallicity environments (e.g. the Magellanic Clouds) form carbon stars at lower masses. Intrinsic S-type stars share many characteristics with carbon stars such as similar masses and a rich s-element chemistry from many dredge-up events, but they lack sufficient carbon to drive the C/O ratio above one.

Stars with masses $\sim 8 - 25\ M_\odot$ do not enter the AGB phase, but become Red Supergiants (RSGs) on the way to ending their lives as Type II supernovae (e.g. Massey & Olsen 2003; van Dyk et al. 2003). RSGs do not

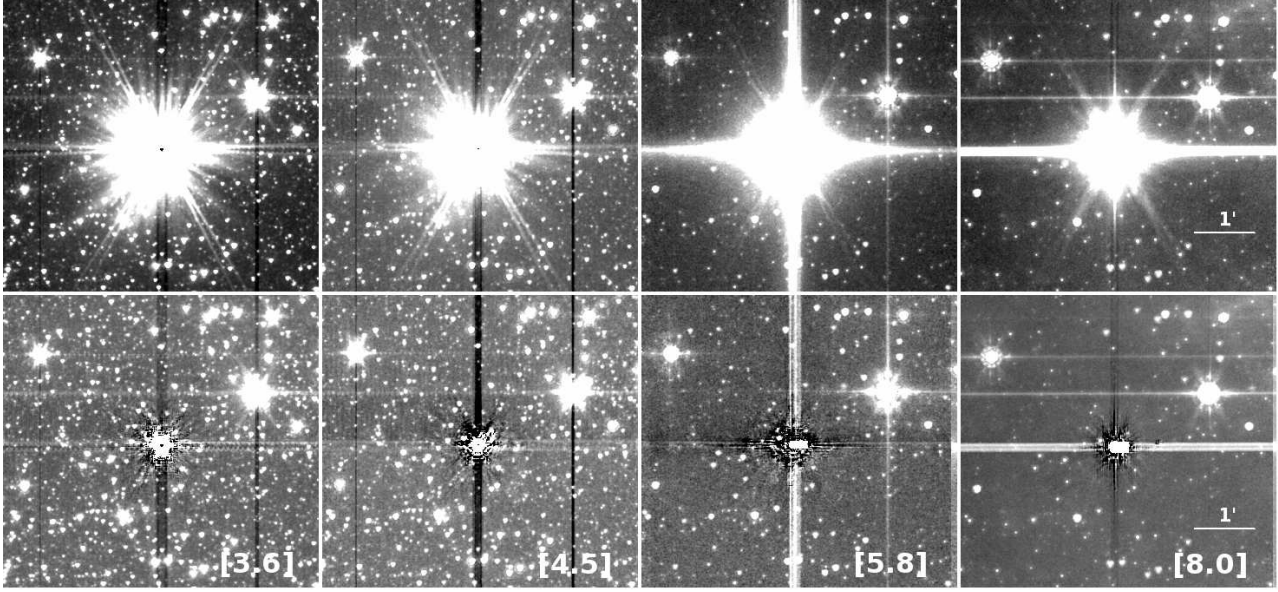


Figure 1. Images of O-rich AGB star CZ Ser in each of the IRAC bands before PSF subtraction (top panels) and after PSF subtraction (bottom panels). The horizontal and vertical bands are un-subtracted electronic artefacts that are ignored in the fit. The PSF was fit to unsaturated diffraction spikes and rings, outside the saturation radius ($\sim 20''$ for CZ Ser). The field of view of each panel is $\sim 5'$.

experience third dredge up episodes and as such they are characterised by an O-rich chemistry (e.g. Verhoelst et al. 2009). More luminous than AGB stars, but with similar spectral types, they are also subject to variability and mass loss. Their dust production rates are comparable to those of AGB stars but their overall yield to the ISM is lower, due to RSGs being more rare than their lower mass counterparts in the AGB (e.g. Boyer et al. 2012).

AGB and RSG stars lie close to an instability region of the Hertzsprung-Russell diagram and as such they exhibit long period variability of Mira, semiregular, and irregular type with periods on the order of hundreds to thousands of days. Period-luminosity diagrams of long period variables (LPVs) in the Magellanic clouds (LMC and SMC) reveal sequences that appear to correspond to the variable pulsation mode, binarity and other as yet unknown characteristics (Wood 2010). These diagrams can be a powerful tool for studying the pulsation mode for a large population of variable stars. This is especially true when the available light curves are sparse and poorly sampled, making it difficult to detect additional periodicity (e.g. overtone pulsations) in the amplitude modulations of the light curve. The construction of similar diagrams for Galactic AGB stars would be extremely useful, as they would illuminate the role of metallicity in determining the pulsation properties of these variables. Efforts in this sense depend critically on accurate and precise distance measurements for Galactic LPVs (Whitelock et al. 2008).

Pulsations and mass loss are inextricably linked in AGB and RSG stars (see e.g. Willson 2000) since radial pulsations aid in the formation of the dust-driven winds responsible for the characteristic high mass-loss rates of AGB stars ($10^{-8} M_{\odot} \text{ yr}^{-1}$ up to $10^{-4} M_{\odot} \text{ yr}^{-1}$, e.g. Wood et al. 1983, 1992; van Loon et al. 1999, as compared with $10^{-9} M_{\odot} \text{ yr}^{-1}$ to $10^{-7} M_{\odot} \text{ yr}^{-1}$, e.g. Mauas et al. 2006; Dupree et al. 2009 for Red Giant Branch stars). The dusty wind that results

from these mass-loss processes, before elements synthesized in AGB stars are released into the ISM, leads to the formation of dusty cocoons enshrouding the star. These circumstellar envelopes obscure optical radiation, making observation of mass-losing AGB stars difficult at visible wavelengths. However, thermal radiation from the dust makes AGB stars extremely luminous in the infrared (IR). The InfraRed Array Camera (IRAC, Fazio et al. 2004) on board the *Spitzer Space Telescope* (Werner et al. 2004) operates in the mid-IR and is an ideal instrument for characterizing AGB stars according to their chemical composition, mass-loss rate, and variability class. IRAC's four channel imaging during the *Spitzer* cryogenic mission was especially well-suited to observe the prominent dust and molecular spectral features in AGB stars – for example, H_2O , SiO , CO_2 , and CO among others for O-rich stars and C_2H_2 , HCN , CS , and C_3 for carbon stars.

Due to their intrinsic brightness and red colors, AGB stars are easily detected by IRAC and have been found in numerous IRAC surveys of the Milky Way (e.g. GLIMPSE, Benjamin et al. 2003; Churchwell et al. 2009) and Local Group galaxies (e.g. SAGE, Meixner et al. 2006; Blum et al. 2006; Boyer et al. 2011). However, there have been no studies specifically designed to characterise in the IRAC bands a sample of Galactic AGB stars with well determined chemical type, variability, and mass-loss rate. To fill this gap, we designed a program to observe a nearby sample of Galactic AGB stars with IRAC in order to better identify AGB stars in IRAC surveys, to facilitate Galactic population synthesis studies, and to better understand the chemical evolution of the diffuse matter in the ISM.

We have observed 48 Galactic AGB stars, representing each of the main types of AGB stars – O-rich, S-type, carbon stars, Mira, semiregular, and irregular variables as well as 6 RSGs of semiregular and irregular variability type. We outline our target selection in Section 2. Section 3 describes

the data reduction pipeline and how the photometry was derived. We present the IRAC colors of AGB stars in Section 4 and discuss period, magnitude and color relations in Section 5. Relationships with the mass-loss rate are explored in Section 6. We summarise our conclusions in Section 7.

2 TARGET SELECTION

Our target list was selected from a number of Galactic AGB star catalogs available in the literature (Loup et al. 1993; Kerschbaum & Hron 1996; Adelman & Maher 1998; Heras & Hony 2005; Guandalini et al. 2006, and references therein) with the intention of representing all main types of AGB stars. Two main constraints limited our choice of targets: (1) the availability of distance estimates and (2) a K band magnitude $\gtrsim 0$, to prevent excessive saturation with IRAC. While our target list is not a statistically significant sample of the Galactic AGB population, the sample is sufficiently large and diverse to allow a general study of the spectral energy distribution (SED) of Galactic AGB stars in the *Spitzer*/IRAC bands, and its overall dependence on their chemical, physical, and variability characteristics.

Distances for our target stars were derived either from interferometric observations (e.g. van Belle et al. 2002; Zhang et al. 2012), models of radio emission and/or bolometric luminosity (Loup et al. 1993; Olofsson et al. 2002; Guandalini et al. 2006; Guandalini & Busso 2008; Schöier et al. 2013), and, in the absence of either of those, astrometric methods (van Leeuwen 2007, adopting the latest corrections of Hipparcos distances). The distance of our selected AGB targets varies from 0.14 to 1.85 kpc (with one single carbon star that has a distance of 4.21 kpc). The distances to previously observed supergiants have been derived with different methods found in the literature (see notes on Table 1).

The complete sample is listed in Table 1, and is divided in three main categories: 22 O-rich AGB stars (M III spectral type), 7 intrinsic S stars, 19 carbon stars, and 6 supergiants. In each category we have a similar number of Mira, semiregular and irregular variables, with periods ranging from 50 to 822 days. Information about the period and variability type of the targets was obtained from the General Catalog of Variable Stars (GCVS, Samus et al. 2012). Estimated mass-loss rates were obtained from radio observations of CO or HCN in the outer envelope, or fitting detailed radiative transfer models of the circumstellar emission to the infrared SED (see Loup et al. 1993; Olofsson et al. 2002; Guandalini et al. 2006, and references therein). The mass-loss rates of our target stars range from 10^{-8} to $10^{-4} M_{\odot} \text{ yr}^{-1}$ in each category. Mass-loss rates for the supergiants were estimated by various methods (see notes in Table 1). Near-IR photometry was obtained (for random epochs) from the 2MASS catalog (Skrutskie et al. 2006). While higher quality near-IR photometry exists for some of the stars in our sample, we chose to adopt 2MASS photometry for uniformity across the sample. The uncertainty of the 2MASS magnitudes are already smaller than the amplitude of the infrared variability of our LPVs. In absence of complete light-curves for all stars in the sample from which to calculate average magnitudes, this obviates

the need for single epoch photometry with better precision than 2MASS.

Given the variability of the sources, we requested two epochs (six months apart, as constrained by the *Spitzer* visibility windows) for each target, in order to check for variations in the IRAC photometry on time-scales of several months.

3 OBSERVATIONS AND DATA REDUCTION

We restricted our target list to nearby AGB stars with estimates of their distance. Given the intrinsic luminosity ($\sim 10^4 L_{\odot}$) and red colors of AGB stars, these targets saturate the IRAC detectors even at the shortest IRAC subarray frame times. While saturated images are not suitable for aperture photometry, reliable photometry can be recovered with Point Spread Function (PSF) fitting, as long as at least part of the PSF is not saturated. To compromise between the need to limit the amount of saturation in our images and, at the same time, fill enough of the IRAC field-of-view with high S/N unsaturated portions of the PSF, we adopted the 2 sec full-frame IRAC Astronomical Observation Template. To allow for efficient removal of outliers (bad pixels and cosmic rays), and sufficient spatial sampling of the unsaturated PSF optical features (diffraction spikes and rings), we observed each target using the 5-point small scale Gaussian dither pattern.

The data were acquired between 2006 June 2 and 2008 June 20 as part of the IRAC Guaranteed Time, with PID 30411. Starting with the Basic Calibrated Data (BCD) produced by the *Spitzer* Science Center (SSC) pipeline version S14.4.0, we generated a mosaiced image for each source, using our own post-BCD software IRACproc (Schuster et al. 2006). IRACproc is an add-on to SSC's MOPEX mosaicing software, that applies more sophisticated outlier rejection criteria. With the optimised parameters from IRACproc, MOPEX defines a fiducial image frame that contains the coordinates for the constituent frames, removes transients using temporal outlier rejection and then interpolates the frames to produce a mosaic image. The final mosaic is scaled to $0.863''/\text{pixel}$ which is $1/\sqrt{2}$ of the IRAC pixel scale (half of the IRAC native pixel area), to provide ideal (Nyquist) sampling even at the shortest IRAC wavelengths.

Table 7 lists the measured IRAC Vega magnitudes for all sources. The adopted PSF fitting technique, developed specifically for heavily saturated IRAC images, is described in Marengo et al. (2009). As an example of this procedure, Figure 1 shows the O-rich AGB star CZ Ser, shown before and after the PSF is fit and subtracted from the target. We used a high dynamic range image of the IRAC PSF¹ in each band, made from a combination of individual images of a set of stars with different brightness (Sirius, Vega, Fomalhaut, ϵ Eridani, ϵ Indi, and the IRAC calibrator BD+68 1022). The PSF intensity is scaled to match the actual IRAC observations of Vega in each band, providing an absolute photometric reference, and is super-sampled over a grid with $0.24''/\text{pixel}$. By fitting the unsaturated parts (diffraction

¹ available at the IRSA website:
<http://irsa.ipac.caltech.edu/data/SPITZER/docs/irac/calibrationfiles/psfprf/>

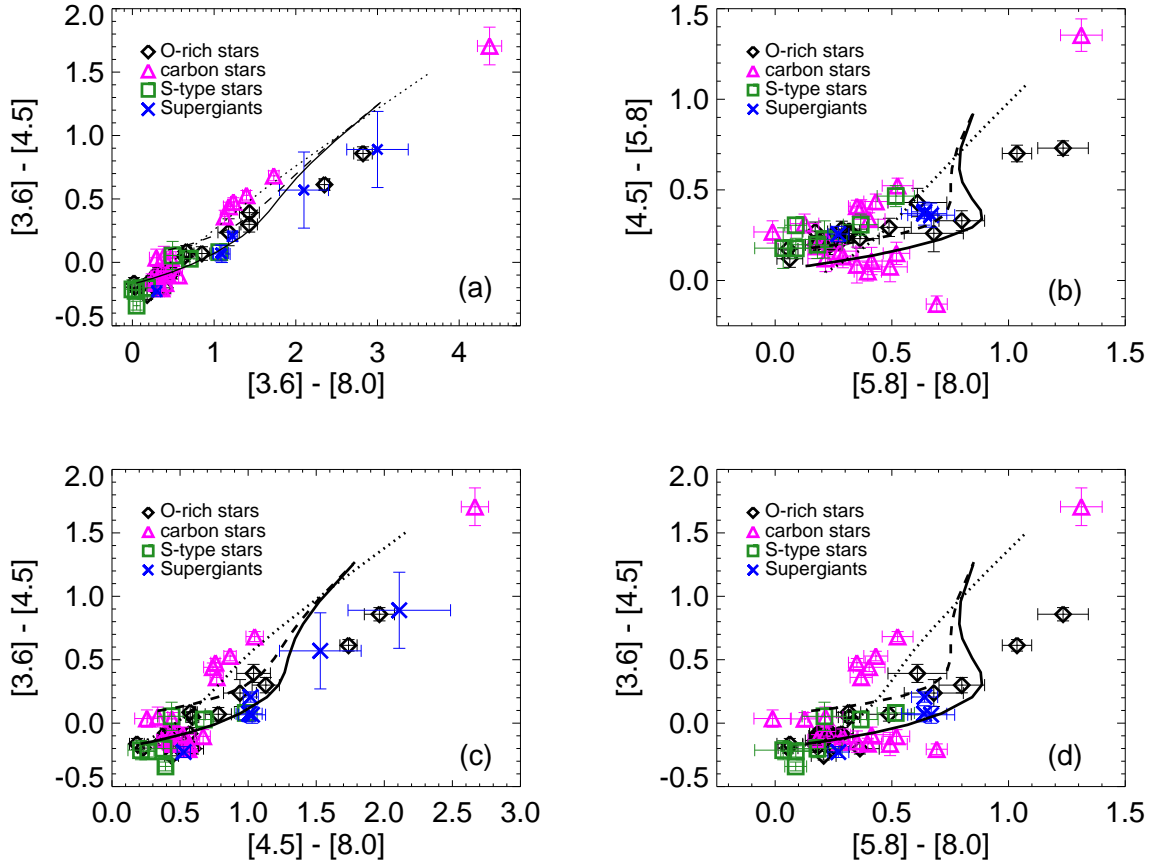


Figure 2. Color-Color diagrams (average of the two epochs) of the observed AGB stars. O-rich stars are marked with diamonds, carbon stars with triangles, intrinsic S-type stars with squares and supergiants with crosses. Model tracks from Groenewegen (2006) for three spectral types are overplotted. Carbon star models are plotted with dotted lines, and models with an M0 III and M10 III central star and silicate dust are plotted with solid and dashed lines, respectively.

spikes and PSF ring and “tails”) of each target star image, we have measured the flux ratio between the stars in our sample and Vega. The typical uncertainty of this procedure is 2–5% (constrained by comparing the amplitude of the PSF subtraction residuals with the background and source photon noise), and is comparable to the typical absolute aperture photometry of unsaturated stars with IRAC. The photometry of the six supergiants from the literature obtained from Schuster (2007) use the same PSF-fitting technique.

4 IRAC COLORS OF GALACTIC AGB STARS

Ground-based mid-IR colors have been used extensively to characterise the physical and chemical properties of the circumstellar envelopes of evolved stars (see e.g. Marengo et al. 1999 and references therein). The IRAC bands offer a similar opportunity, as they span a wavelength range rich in strong molecular and dust features, and they are free from variable telluric absorption lines. These features correlate with the chemical signature of the circumstellar environment, dust mineralogy, and abundance in the stellar wind. Note that in the IR, interstellar extinction is dramatically

reduced with respect to the visible; as a consequence the mid-IR and near-IR colors of our sources are mainly determined by photospheric and circumstellar features.

Figure 2 shows a number of IRAC color-color diagrams for all target sources. Each source is plotted once, using the average color of the two observed epochs. The sources tend to be organized on a sequence of increasing excess colors, matching the overall distribution of colors found by Marengo et al. (2007) using synthetic IRAC photometry derived from Infrared Space Observatory Short Wavelength Spectrometer (ISO SWS, Valentijn et al. 1996) spectra (from Sloan et al. 2003). The largest dispersion is in the $[3.6] - [8.0]$ color (panel *a*). Radiative transfer models (see e.g. Groenewegen 2006) show that this sequence is related to increasing amounts of circumstellar dust, indicating larger mass-loss rates (assuming wind velocities, dust opacities, and a uniform dust-to-gas mass ratio across the sample). We explore quantitatively the correlation between mass-loss rates and IRAC colors in section 6.

Stars extending along the infrared excess sequence tend to separate according to their circumstellar chemistry. O-rich and intrinsic S-type AGB stars, as well as the supergiants, tend to have a redder $[3.6] - [8.0]$ color (for the same $[3.6] - [4.5]$ color), due to the presence of silicate features dra-

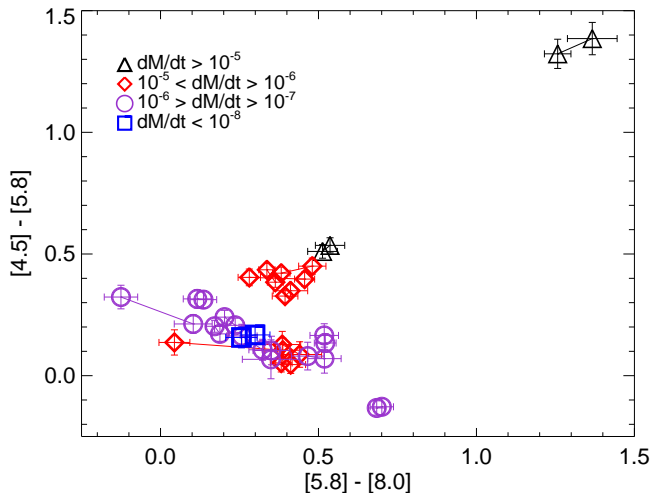


Figure 3. Color-color diagram of our carbon stars with different symbols for increasing mass-loss rate. For each star we show the color for both epochs, connected by a line. Stars with the highest mass-loss rates are on the upper branch, with redder $[4.5] - [5.8]$ color than the lower branch. Stars with lower mass-loss rates are on the lower track, indicating depressed flux at $5.8 \mu\text{m}$.

matically increasing their flux in the $8.0 \mu\text{m}$ band. This separation is only effective for sources with moderate infrared excess, e.g. $[3.6] - [8.0] \gtrsim 1 \text{ mag}$.

The Groenewegen (2006) models we selected miss the location of the most extreme O-rich AGB stars in all of the color-color diagrams. This may be due to the choice of dust chemistry in the model. In Figure 2, we plot models using a mixed chemistry – 60% aluminum oxide (amorphous porous Al_2O_3) and 40% silicates (see Groenewegen 2006, for details). More recent papers have shown that the choice of optical constants affects the predicted flux of the silicate feature near $10 \mu\text{m}$ (see Groenewegen et al. 2009). This suggests that the particular silicate opacities employed in the model may lead to the inaccurate determination of the dust mass-loss rate.

Plots including colors with the $5.8 \mu\text{m}$ band (panels *b* and *d*) instead show an unexpected separation of carbon stars into two distinct branches. Both branches show similar $[5.8] - [8.0]$ excess, but the upper branch continues to get progressively redder in both $[4.5] - [5.8]$ and $[3.6] - [4.5]$ colors, whereas stars in the lower branch tend to get bluer in the $[4.5] - [5.8]$ color. This divergence suggests the presence of a broad absorption feature at $5.8 \mu\text{m}$. Looking at just the carbon stars in $[5.8] - [8.0]$ versus $[4.5] - [5.8]$ color and using different symbols to indicate increasing mass-loss rate (Figure 3), we see that the separation is related to the mass-loss rate listed in Table 1. Stars with higher mass-loss rates are on the upper, red branch, while stars with lower mass-loss rates populate the lower, blue track. This dichotomy suggests that the feature responsible for the $5.8 \mu\text{m}$ absorption is likely photospheric, being masked by thicker dusty envelopes in sources with higher mass-loss rates.

To identify this feature, and to match the observed trends in the IRAC colors with specific spectral features, we retrieved archival spectra (Sloan et al. 2003) for all of our sources that were observed with ISO SWS. We have

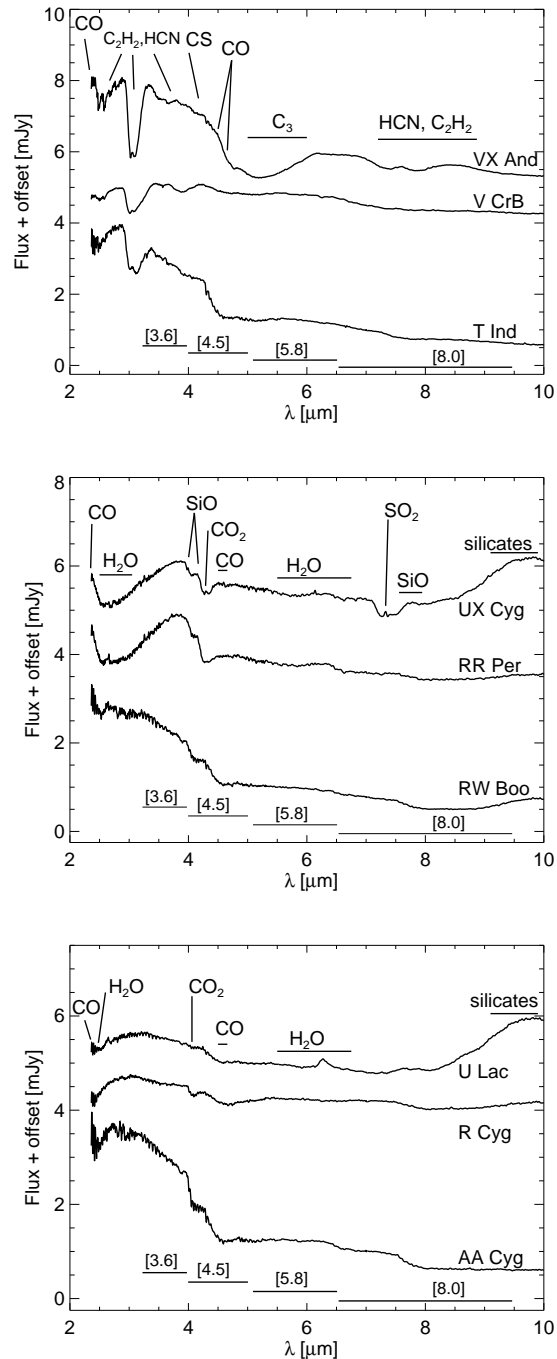


Figure 4. ISO SWS spectra of representative stars in our sample. *Top:* – carbon stars; *Center:* – O-rich AGB stars; *Bottom:* – two intrinsic S-stars and a red supergiant (AA Cyg). The IRAC passbands are plotted below the spectra and the main photospheric and circumstellar features are indicated (following, e.g. Aoki et al. 1999; Noriega-Crespo et al. 2004; Zhang & Jiang 2008).

also compared our colors with the synthetic photometry of 122 AGB and RSG stars of different chemical type, derived by Marengo et al. (2007) by convolving available ISO/SWS spectra with the IRAC passbands. Some of these sources have been observed by ISO at multiple epochs allowing a direct test of the effect of variable spectral features on the

IRAC colors. Representative examples are shown in Figure 4. The spectrum of carbon stars along the blue branch (e.g. VX And in the top panel) exhibits a strong C_3 absorption feature centred at $5\ \mu\text{m}$. This feature is not present in the spectra of stars in the redder branch (e.g. V CrB and T Ind). Based on Sloan & Price (1998), C_3 is assumed to be developing in the atmospheres of dust poor carbon stars. This feature disappears in stars with thicker circumstellar envelopes, either because it is filled by the continuum dust emission, or because the molecule making the feature is depleted. As noted in Marengo et al. (2007), this feature appears to be transient, as some sources observed with ISO SWS in multiple epochs do not show it in all spectra. This suggests that the feature variability is related to changes in the C_3 abundances in the stellar atmosphere as the star pulsates, rather than changes in the dust content of the circumstellar envelope (which is unlikely to show large scale variations on the short time-scales of the ISO repeated observations, although such variations are found on longer time-scales, see e.g. Whitelock et al. 2006).

The spectra of carbon stars present several other molecular features in the IRAC passbands (CO , C_2H_2 , HCN and CS). C_2H_2 falls mostly outside the $3.6\ \mu\text{m}$ band, and does not contribute significantly to the $[3.6] - [4.5]$ color of the carbon stars. CO absorption in the $4.5\ \mu\text{m}$ band more likely contributes to the negative (as low as $\simeq -0.2\ \text{mag}$) $[3.6] - [4.5]$ color of the carbon stars with low overall infrared excess. All these molecular absorption features are filled by dust continuum emission for the redder sources, explaining the general trend of increasing $[3.6] - [8.0]$ color for stars with larger circumstellar dust content.

The mid-IR spectra of the O-rich sources (middle panel), intrinsic S-stars and a red supergiant (bottom panel) are also rich in several molecular features (including CO , H_2O , SiO , CO_2 and SO_2). Of these, the features that have the largest effect on the IRAC colors are SiO , CO_2 , and CO bands that can severely depress the $4.5\ \mu\text{m}$ flux leading to blue $[3.6] - [4.5]$ colors (as low as $\sim -0.4\ \text{mag}$) for the sources with less overall infrared excess. Sources with high dust content show the prominent $10\ \mu\text{m}$ silicate feature in emission. As mentioned before, this feature is partially captured by the $8.0\ \mu\text{m}$ band, causing the $[3.6] - [8.0]$ color to be redder for higher mass-loss rates. There are no significant differences between the colors of the individual types of O-rich sources, as evidenced by the fact that M-type AGB stars, intrinsic S-stars and red supergiants all trace the same color sequence.

A number of classification schemes for the chemistry of AGB stars rely on the combination of IRAC with near-IR colors. Figures 7 and 8 in Boyer et al. (2011), for example, show how O- and C-rich sources in the SMC and LMC segregate according to their $J - [8.0]$ color. With this scheme, O-rich AGB stars have $J - [8.0] \lesssim 1.4\ \text{mag}$ and C-rich AGB stars have $J - [8.0] \gtrsim 1.9\ \text{mag}$, with the so-called “anomalous” O-rich population having intermediate color. We do not see this segregation for Galactic AGB stars, as shown in our Figure 5, where C-rich and O-rich AGB stars overlap above $J - [8.0] > 2\ \text{mag}$ and intrinsic S-type stars (proposed as one possible explanation for the LMC/SMC anomalous O-rich AGB class) overlap with the range of the anomalous O-rich AGB stars (see box in Figure 5).

The fact that we have several O-rich AGB stars that

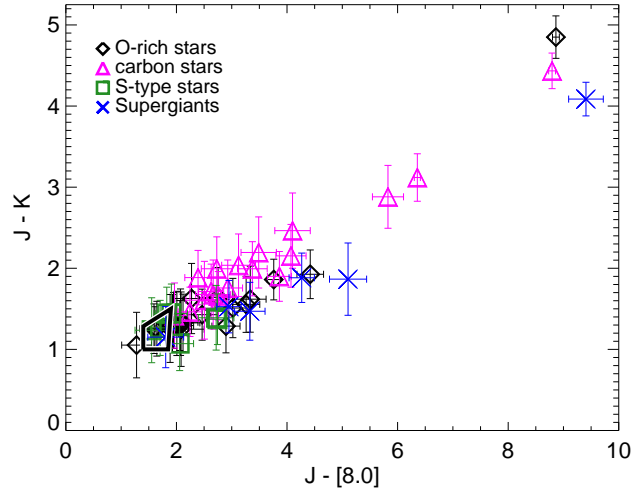


Figure 5. Color-magnitude diagram using near-IR photometry from 2MASS and Spitzer $8\ \mu\text{m}$. The trapezoidal box frames anomalous O-rich AGB stars as identified by Boyer et al. (2011).

have significantly redder colors than most O-rich AGB stars in the Magellanic Clouds may be the consequence of the different evolutionary paths of the two AGB populations in galaxies with different metallicity. AGB stars are observed to have redder colours at higher metallicities because the gas to dust ratio increases (van Loon 2000). We note that the few O-rich AGB stars in the Magellanic Clouds that have redder colours than the Galactic AGB stars in our sample are OH/IR stars (Wood et al. 1992; Marshall et al. 2004). As noticed by many authors (see, e.g. Ferrarotti & Gail 2006; Ventura et al. 2012) a low metallicity environment favors the creation of carbon stars early in the evolution of an AGB star, when the mass-loss rate (and hence infrared excess) tends to be smaller. According to this hypothesis, LMC/SMC O-rich AGB stars are restricted to low $J - [8.0]$ excess, with only C-rich stars having redder $J - [8.0]$ colors due to their greater mass loss. This restriction would not be present in Galactic O-rich AGB stars, requiring a higher number of thermal pulses to transition to C-rich chemistry. Alternatively (though not in our sample), the neat color separation observed in the LMC/SMC C- and O-rich AGB stars could be explained by the selection method used to identify the chemical type of the source. LMC/SMC AGB catalogs are typically based on near-IR colors (see e.g. Figure 5 in Boyer et al. 2011) while the chemistry of our targets has been identified spectroscopically. This second possibility is supported by the large range in infrared colors exhibited by spectroscopically identified C- and O-rich LMC AGB stars (see e.g. Matsuura et al. 2009). Finally, this may be a selection bias in our sample as we have selected sources with measurable mass-loss rates, and hence a larger infrared excess.

The two reddest O-rich AGB stars in our sample are KU And and V1300 Aql. Both have red $[3.6] - [8.0]$ color and V1300 Aql is the reddest in the near-IR (consistent with its fainter J-band magnitude indicative of higher circumstellar extinction, see Table 1). Several (5) of our O-rich AGB stars have $[5.8] - [8.0]$ vs. $[3.6] - [4.5]$ color sufficiently red that

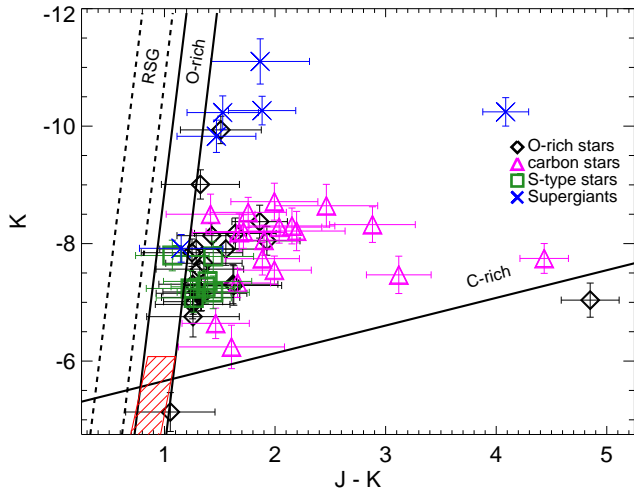


Figure 6. Color-magnitude diagram using near-IR photometry from 2MASS. Lines correspond to the near-IR color cuts used by Boyer et al. (2011). The red striped box denotes the RGB.

they would be considered *extreme* AGB stars by Boyer et al. (2011). In fact, all of our O-rich AGB stars are redder than the $J - K$ color cut Boyer et al. (2011) use to isolate O-rich AGB stars in the LMC (see Figure 6).

To test whether the redder colors of our O-rich AGB stars are representative of the Galactic AGB population, or rather are the consequence of selection effects, we extracted the 2MASS photometry of all Mira and semiregular variables in the GCVS (Samus et al. 2012) with known chemical type. The median $J - K$ color (0.85 mag) of this larger sample of O-rich AGB stars falls within the Boyer et al. (2011) color cut, suggesting that the red colors of the O-rich AGB stars reflect our choice of O-rich AGB stars with measured mass-loss rates, and thus greater IR excess (see Figure 7). It should be noted, however, that a large fraction of the GCVS carbon stars have a $J - K$ color falling outside the boundaries of the Boyer et al. (2011) C-rich color cut. Javadi et al. (2011) also find that carbon stars are less red at similar metallicities in M33. We find that 78% of the C-rich AGB stars in the Galaxy are bluer than $J - K \sim 1.2$ mag (the color selection criteria from Boyer et al. 2011, for $K \sim -8$ mag, see Figure 6). Based on this, the majority of C-rich sources would likely be misclassified as O-rich sources. However, sources in the GCVS tend to be optically selected, and as such are biased toward low circumstellar extinction (small mass-loss rates), and may sample less-evolved, non-dusty AGB stars that behave very differently than their more evolved, dustier counterparts (Boyer et al. 2011).

4.1 Source Variability

The availability of two separate epochs, while not sufficient to reconstruct a full light-curve, is enough to estimate the average variations of LPVs in the IRAC bands. Figure 8 shows the histograms of the average magnitude change between epochs for all sources in our sample. The RMS variations are 0.29, 0.28, 0.27, and 0.26 mag at 3.6, 4.5, 5.8 and 8.0 μm respectively. This is much larger than the RMS variations

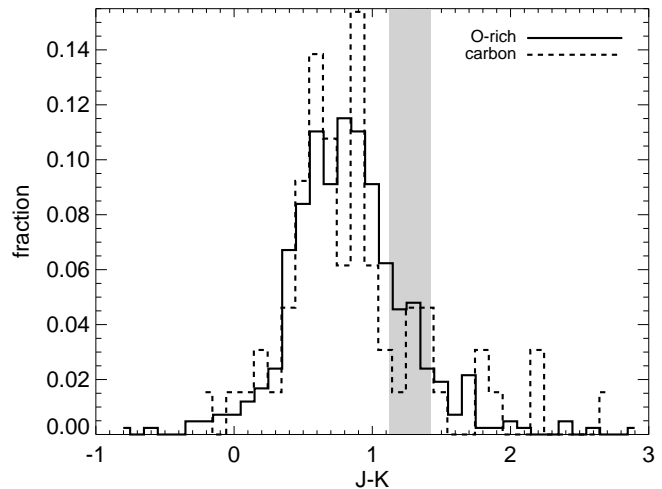


Figure 7. Histogram of the $J - K$ color of all AGB stars of known chemical and variability type from the GCVS. J and K photometry from 2MASS. The shaded region indicates the $J - K$ color range of the O-rich AGB stars in the Boyer et al. (2011) color selection.

expected for a sample of non-variable stars ($\lesssim 0.008$ mag for all bands), based on the average photometric uncertainty. As expected, the IRAC bands are affected by the variability of the sources to a much smaller extent than the optical bands (where Mira light-curves can have amplitudes as large as 11 mag, Samus et al. 2012), with smaller variations for longer wavelengths. The smallest changes are observed for sources that are classified as semiregular or irregular variables (0.14, 0.12, 0.11, and 0.10 mag in each band), as expected because of their shorter periods and smaller pulsation amplitudes with respect to Miras (0.46, 0.45, 0.42, and 0.41 mag respectively).

The IRAC color changes between epochs are generally small ($\text{RMS} \simeq 0.08$ mag), resulting in a small scatter in the color sequences shown in Figure 2. The largest variation is found in the $[5.8] - [8.0]$ color for the carbon stars in the blue branch ($\text{RMS} \simeq 0.11$ mag), affected by the variability of the C_3 feature (see figure 3). One carbon star (RS Cyg) also shows a first epoch $[3.6] - [8.0]$ color significantly bluer (by 0.31 mag) than all other carbon stars. Unfortunately, ISO SWS spectra are not available for this source. However, we found that our second epoch IRAC photometry closely fits the spectrum of another carbon star, T Ind. The first epoch IRAC photometry of RS Cyg is characterised by a much higher 3.6 μm flux than the second epoch, or the T Ind spectrum. We suspect that this fluctuation is due to unusually strong, variable C_2H_2 absorption, common in many of the ISO SWS spectra of the other carbon stars in our sample. L and M band spectra of RS Cyg taken at multiple phases would be required to confirm this hypothesis, and the existence of such broad variations in the strength of this absorption feature.

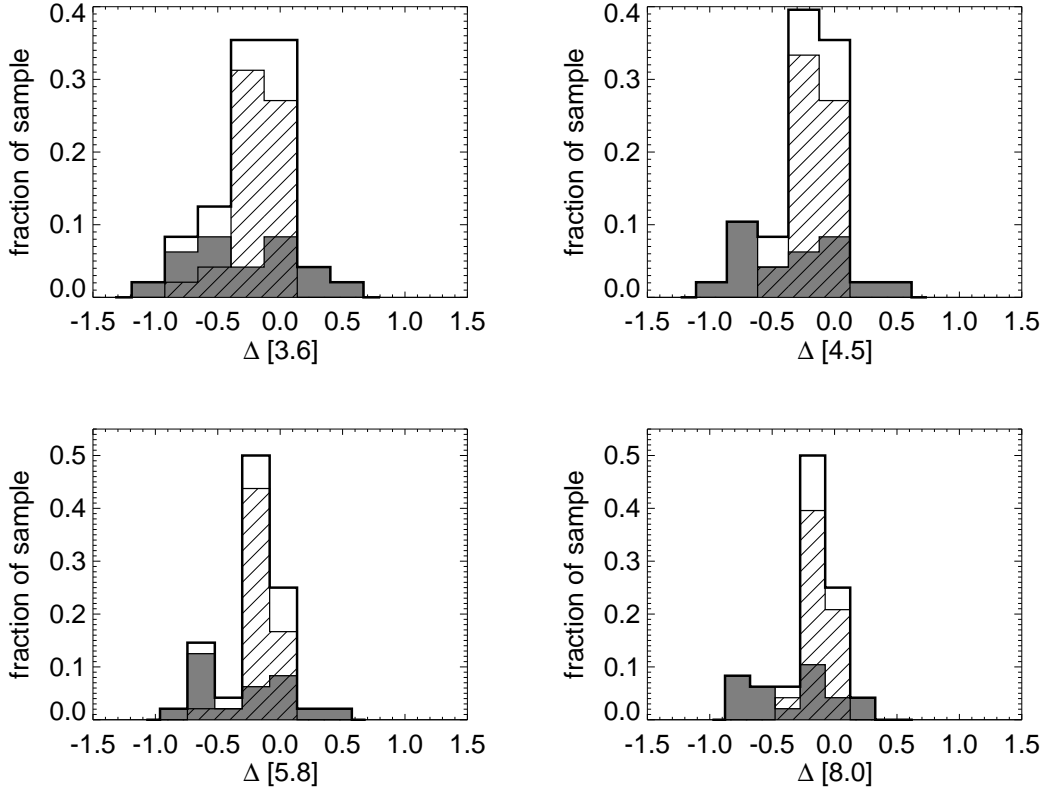


Figure 8. Histogram of the magnitude variations between the two epochs of observation. White boxes show variations of the full AGB sample, with Mira variables indicated with gray boxes, semiregular and irregulars indicated with striped boxes.

5 PERIOD, MAGNITUDE AND COLOR RELATIONS

LMC and SMC LPVs tend to organize themselves in a series of parallel sequences in optical and infrared period-luminosity diagrams (see e.g. Wood 2010; Riebel et al. 2010 and references therein). These sequences depend on the pulsation mode, binarity, and other not yet identified parameters (giving rise to poorly understood characteristics, like a long secondary period observed in some stars). The so-called *C* sequence is populated by fundamental mode pulsators. The brightest of the *C* sequence variables tend to be Miras, while the lower end of the sequence (straddling the RGB tip) is mainly inhabited by semiregulars. Sequence *C'* (to the left of sequence *C* by $\Delta[\log P] \simeq -0.1$), is instead populated by first overtone semiregular variables. LPVs with higher overtone modes are organized in separate sequences (*A* and *B*) with even shorter periods. Stars with the mysterious secondary long period are found in sequence *D*, shifted by $\Delta[\log P] \simeq +0.3$ from the *C* sequence.

Figure 9 shows the period-luminosity diagram calculated for the 3.6 μm absolute magnitude (averaged between the two epochs) for our sample of AGB stars. Diagrams for the other three bands are similar. The sources classified in the GCVS (Samus et al. 2012) as Mira and semiregulars are indicated by different symbols. The size of the symbols is proportional to the [3.6]–[8.0] color (as a proxy for their mass-loss rate). The shaded bands for the individual sequences are derived from the approximate distribution of

LMC LPVs in Riebel et al. (2010) where the [3.6] magnitude is taken as a proxy for the luminosity, and converted to absolute magnitudes using the LMC distance modulus of 18.5 (Freedman et al. 2001; Walker 2011). These sequences are similar to those found by Wood (2010) using the *K* band magnitude as a proxy for luminosity, however they have a slightly shallower slope (larger period for a given luminosity).

The location of our sources on the diagram is listed in Table 3 and is largely as expected, based on AGB stars in the Magellanic Clouds, confirming results found by Glass et al. (2009) using synthetic IRAC photometry from Marengo et al. (2007). Miras (squares) are all within or below the sequence *C* (fundamental pulsators), with the exception of the carbon star R For, which is in the first overtone sequence *C'*. A few of the Miras appear to be significantly under-luminous in the 3.6 μm band, up to 3 mag below the *C* sequence for their period, placing them in or near the secondary long period sequence *D*. Most of these stars (e.g. KU And and V1300 Aql) have large infrared excess due to their high mass-loss rate; their low 3.6 μm brightness may be caused by the large extinction due to their thick circumstellar envelope. Alternately, they may have increased their period as the stellar structure responds to the mass lost. The semiregular variables, as expected, are mostly located in the overtone sequences or the lower part of sequence *C*. Only four semiregulars (T Ind, VX And, BN Mon and RS Cyg, all carbon stars) are found in the area of the *C* sequence oc-

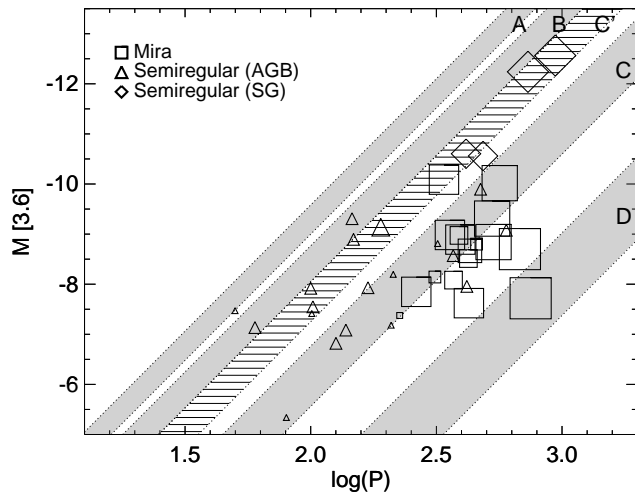


Figure 9. 3.6 μm absolute magnitude (average of the two epochs) versus the logarithm of the period in days for all Miras (squares), semiregular AGB variables (triangles), and supergiants (diamonds) with a period available in the literature. Shaded and striped boxes indicate the approximate distribution of LMC LPVs in Riebel et al. (2010). Symbol sizes correspond to $[3.6] - [8.0]$ color (taken as a proxy for their mass-loss rate).

cupied by fundamental mode Miras. ET Vir is the faintest source in the plot, lying at the very bottom of sequence *C*. At a Hipparcos-determined distance of 0.14 kpc, ET Vir is also the nearest source in the sample. Given the large uncertainty on the parallax ($> 30\%$), we might expect that the luminosity has been underestimated due to an unreliable distance estimate. However, the Hipparcos value agrees well with the distance modulus calculated using the width of chromospheric Ca II emission lines (Wilson 1976) to determine the absolute magnitude, making it unclear why ET Vir is more than a magnitude fainter than the other sources in the sample. One possibility is that we observed ET Vir with lower luminosity following a thermal pulse. All semiregular AGB variables in our sample tend to have small infrared excess, so it is unlikely that their position in the diagram is significantly affected by extinction at 3.6 μm . The only semiregular variables with large excess are four supergiants (XX Per, W Per, NML Cyg, and VX Sgr), located at the top of sequence *C'* as expected.

The general distribution of our Galactic LPVs in the period-luminosity diagram is characterised by a significantly larger spread than the variables in the Magellanic Clouds. As found by previous authors (see e.g. Tabur et al. 2010), this is primarily due to the larger uncertainty in the distance of Galactic LPVs, and possibly in the larger spread in their metal abundance, which also affects their period-luminosity relation. Despite these difficulties, the period-luminosity plot using the IRAC 3.6 μm band (where extinction is minimal, and infrared excess tends to be lower than at longer wavelengths) as a proxy for luminosity remains an important tool to study the pulsation mode of these variables, most of which only possess sparse and incomplete light-curves.

While period-magnitude relations are diagnostics of the pulsation mechanisms of several classes of variables, the in-

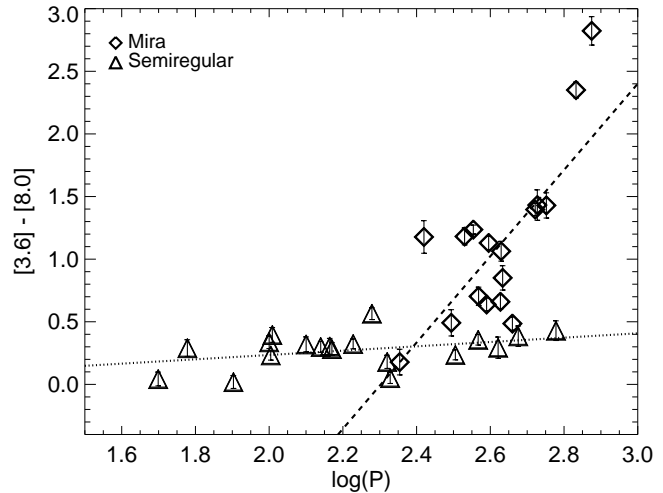


Figure 10. IRAC $[3.6] - [8.0]$ color (average of the two epochs) versus the logarithm of the period in days. A fit to the semiregular variables (triangles) shows a strong correlation with period (dotted line). A fit to the Miras (squares) is less well-defined (dashed line).

frared colors of AGB stars are dominated by dust emission and molecular absorption. The relationship between infrared colors and period, however, provides an excellent diagnostic to investigate the dependence of the circumstellar chemistry and mass-loss rate on the pulsation period. The $[3.6] - [8.0]$ color, which is strongly affected by dust emission, is a good candidate for this analysis.

The results are shown in figure 10. Semiregular variables are distributed along a tight ($\text{RMS} \simeq 0.12 \text{ mag}$) period-color relation, statistically consistent with a zero slope, confined within a narrow color range ($\Delta([3.6] - [8.0]) \lesssim 0.5 \text{ mag}$). Note that all semiregulars, including the ones with larger period that appear to be on the fundamental mode sequence *C*, are part of the same period-color relation. The Mira variables are instead spread over a much larger range of colors ($\Delta([3.6] - [8.0]) \approx 3 \text{ mag}$), with longer period sources (on the *D* sequence) having the largest infrared excess. The two linear best-fitting relations are:

$$\begin{cases} \text{Semiregular} \\ [3.6] - [8.0] = (-0.11 \pm 0.10) + (0.17 \pm 0.05) \log(P) \\ \text{RMS} = 0.12 \text{ mag} \end{cases} \quad (1)$$

$$\begin{cases} \text{Mira} \\ [3.6] - [8.0] = (-7.93 \pm 0.41) + (3.45 \pm 0.16) \log(P) \\ \text{RMS} = 0.42 \text{ mag} \end{cases} \quad (2)$$

where the period is in days.

One possible explanation for this dichotomy is that the two groups of variables are characterised by different dust composition, affecting their excess in the IRAC bands. One problem with this interpretation is that there seems to be no difference between O-rich (M and S-type) and C-rich AGB stars, despite the very different source of the infrared excess (mainly continuum from amorphous carbon dust for carbon stars, and the 10 μm silicate feature in emission for M and S-type AGB stars). Another possibility is a difference in the amount of circumstellar dust responsible for the IR excess,

i.e. a different mass-loss rate. While the median mass-loss rate of the Miras in our sample is indeed higher than for the semiregulars (2.1×10^{-6} and $4.6 \times 10^{-7} M_{\odot} \text{ yr}^{-1}$ respectively), the separation is not as marked as in the color-period space. A third possibility is that the separation in color reflects different circumstellar dust temperatures. Given that the IRAC bands are sensitive to dust in the temperature range 500 – 800 K, the observed dichotomy may indicate that semiregulars are deficient in the hot dust emission that is present in Mira variables. This is consistent with the suggestion in Marengo et al. (2001) that semiregular variables could have discontinuous mass-loss, spending a significant part of their time in the quiescent phase with only brief phases of higher mass-loss. According to this hypothesis, semiregulars would have more excess during these brief intervals of higher mass-loss, but once this phase has concluded, the dust would expand and cool, leading to a small $[3.6] - [8.0]$ excess ($\lesssim 0.5$ mag). Infrared color variations due to intermittent dust production have been found for many AGB stars (see e.g. Whitelock et al. 2006, and references therein), for both Mira and semiregular LPVs. Those variations have been attributed to the emission of dust clumps, similar to the ones observed with interferometric observations of the very obscured Mira carbon star IRC+10216 (Tuthill et al. 2000). The different color we observe between Mira and SR variables may reflect the fact that dust episodes in semiregulars happen on longer time-scales, giving the dust time to cool between each mass-loss episode. Less excess for the semiregulars would mean that their IRAC colors are a better reflection of the star's intrinsic color (and not thermal emission from the dust). This would lead to the more strict period-color relation for semiregular than for Mira variables. Indeed it is the higher excess in Mira variables that would prevent a similarly tight relation.

6 MASS LOSS AND COMPARISON TO LMC/SMC AGB STARS

The intense mass-loss processes that are often active during the AGB phase are not well understood. Commonly used empirical mass-loss-rate formulas (see e.g. Salpeter 1974; Reimers 1975; Baud & Habing 1983; Nieuwenhuijzen & De Jager 1990; Vassiliadis & Wood 1993) only provide an order-of-magnitude estimate of the mass-loss rate of AGB stars and cannot predict the actual mass-loss rate as a function of stellar parameters. Radiative transfer modeling can be used to infer the amount of circumstellar dust from excess flux measurements in the thermal infrared. Coupled with assumptions about the AGB wind velocity (usually $\sim 10 - 20 \text{ km s}^{-1}$) and the gas-to-dust mass ratio (typically in the range of the ISM ratio of ~ 200), these models can be used to provide estimates for AGB mass-loss rates from infrared photometric measurements. This can be achieved either by fitting the SED (see e.g. Gullieuszik et al. 2012; Riebel et al. 2012) of each source to a model or adopting a color – mass-loss relation (see e.g. models using realistic stellar atmospheres from Groenewegen 2006; Groenewegen et al. 2009, 2007; Gruendl et al. 2008). These models show how high-mass-loss rate AGB stars of all types follow monotonically increasing sequences similar

to those shown in Figure 2 (higher mass-loss rate, stronger infrared excess).

Figure 11 shows the mass-loss rate plotted as function of $[3.6] - [8.0]$ color. Reflecting the color separation found in Figure 10, all semiregular variables are grouped in the 0 – 0.5 mag color range. However, the overall mass-loss rates are comparable for the two groups. This is in accordance with the previously mentioned results found in Marengo et al. (2001; see discussion in Section 5), and since we would expect semiregular variables to show less excess than Mira variables if they are characterised by discontinuous mass-loss.

The overlap in the distribution of AGB stars of different chemical types echoes our finding that the majority of O-rich AGB stars in our sample have colors consistent with carbon stars (see Section 4). Because our sample of O-rich AGB stars is biased towards higher mass-loss rates, the most significant contributors of O-rich AGB dust are also the most likely to be mis-classified with color cuts alone, suggesting that care must be taken in inferring the chemical yield of AGB dust from color-selected stellar population studies.

Selecting for AGB stars with measured mass-loss rates may also explain the relatively high mass-loss rate that is characteristic of our sample. Our best-fit for the mass-loss rate as a function of $[3.6] - [8.0]$ color for the O-rich AGB (excluding the supergiants) and C-rich AGB samples respectively, are:

$$\begin{aligned} \text{C-rich :} \\ \log(dM/dt) &= -19.20 / ([3.6] - [8.0]) + 3.65 - 1.45 \\ \text{O-rich :} \\ \log(dM/dt) &= -9.65 / ([3.6] - [8.0]) + 1.35 - 2.29 \end{aligned} \quad (3)$$

While the small number of sources in either sample does not allow us to establish meaningful uncertainties to the fits, we note that the two curves approach each other for $[3.6] - [8.0] \gtrsim 2$ mag. This suggests that the mass-loss rate for red sources is similar, for a given value of the infrared excess, regardless of the dust chemistry. Our three supergiants with reliable mass-loss rate estimates follow a trend similar to the AGB stars, but as expected are shifted towards higher mass-loss rates.

Similar fits are provided by different authors for AGB stars in the Magellanic Clouds. Figure 11 shows a selection of them (Matsuura et al. 2009, 2013; Gullieuszik et al. 2012; Riebel et al. 2012), based on the photometry obtained as part of the *Spitzer*/IRAC SAGE program. It is worth noting that the spread between the individual fits is large, as much as an order of magnitude in dM/dt . This spread may be, in part, a consequence of the specific selection criteria adopted by different authors, leading to different biases in the AGB samples used in the fit. Different assumptions for the gas-to-dust ratio and wind velocity, as well as different optical constants used to model the sources will also contribute to the spread. While our best-fitting relations predict larger mass-loss rates for our Galactic AGB sample, the large uncertainty in the fit parameters and the spread between the Magellanic Cloud curves prevent us from deriving meaningful conclusions about the dependence of mass-loss rates on metallicity. Such a dependence is expected for O-rich AGB stars, but not for C-rich sources, since carbon is synthesized locally in the Thermally-Pulsing AGB stars, as argued by Matsuura et al. (2009). However, it is unclear whether the

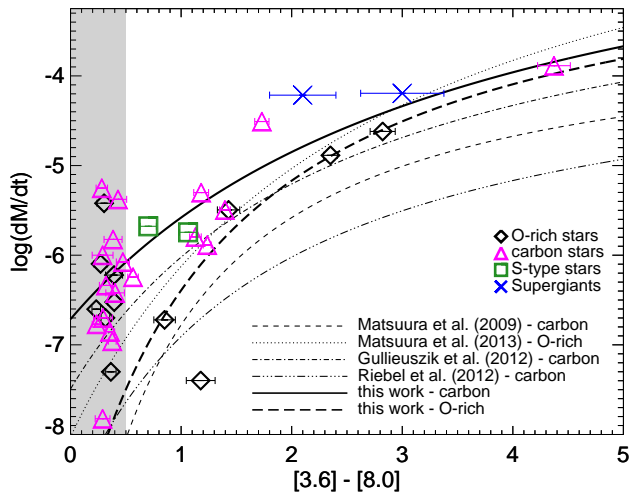


Figure 11. A comparison of fits to the mass-loss rate as a function of $[3.6] - [8.0]$ color. The best-fitting relations to our sample of Galactic C- and O-rich AGB stars are shown with bold straight and dashed lines respectively. These are compared to fits found by other authors for larger samples of AGB stars in the LMC. Semiregular and irregular LPVs fall within the shaded region while the Mira variables all have redder color.

local synthesis of carbon increases the dust-to-gas ratio (see, e.g. van Loon et al. 2008). A large Galactic sample with reliable distances (that could be provided in the near future by GAIA) and radio-based mass-loss rate determinations will help resolve this issue.

The selection criteria used by Matsuura et al. (2009, 2013) to differentiate evolved stars in the Magellanic Clouds result in a sample that is more directly comparable with our own Galactic sample. The sources in these works are identified by optical and infrared spectroscopy, avoiding the potential mis-classification of red O-rich sources (OH/IR stars and RSG) in the extreme AGB class (where most of the sources, at least in the Magellanic Clouds, are C-rich). Matsuura et al. (2013) show how spectrally classified sources of different type tend to separate into three different regions in the $[3.6] - [8.0]$ versus $[8.0]$ color-magnitude diagram. These three regions are overlaid on our sample in Figure 12. Note that for our Galactic sources, the bright supergiants also have the highest mass-loss rate plotted in Figure 11. Our two O-rich AGB stars with larger infrared excess are in the lowest luminosity region in the Matsuura et al. (2013) diagram, within the region where extreme C-rich AGB stars are expected. However, these two stars are characterised by a mass-loss rate as high as C-rich AGB stars with similar excess. As pointed out by Matsuura et al. (2013) and Riebel et al. (2012), the overall dust return of AGB stars to the ISM of the Magellanic Clouds is dominated by a handful of stars with very large mass-loss rates. In the Magellanic Clouds, most of these stars tend to be C-rich ‘extreme’ stars. The situation may be different in the Galaxy where a large number of very red OH/IR stars are found. These O-rich evolved stars, with mass-loss rates as high as the two reddest O-rich AGB stars in our sample, may contribute as much as the C-rich AGB stars to the overall dust budget in our Galaxy. A larger por-

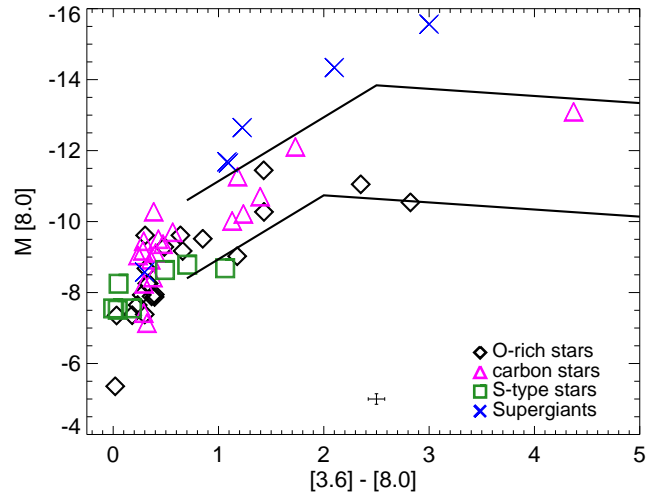


Figure 12. Color-Magnitude diagram of IRAC band $[8.0]$. Average error is plotted in bottom centre. Color-magnitude selection cuts from Matsuura et al. (2009) overplotted.

tion of O-rich AGB stars with high mass-loss rates in sources with near solar metallicity has indeed been observed in M33 (Javadi et al. 2013).

7 CONCLUSIONS

We present the results of the first study to characterise Galactic AGB stars in the IRAC bands. The sample consists of 48 AGB stars observed in two epochs – 22 O-rich, 19 carbon-rich, and 7 S-type – representing a diverse AGB population with well-determined distance, chemistry, variability type, and mass-loss rate. These are compared to 6 supergiants representing mass-losing evolved stars outside the AGB.

By fitting a PSF to unsaturated parts of the IRAC images, we derive reliable photometry in all four IRAC bands. From this, we compute the mid-IR colors of Galactic AGB stars. AGB stars with O-rich chemistry (including S-type AGB stars) tend to have redder $[3.6] - [8.0]$ colors than carbon stars for a given $[3.6] - [4.5]$ color, possibly driven by silicate emission in the $[8.0]$ band. For colors including the $5.8 \mu\text{m}$ band, carbon stars separate into two distinct sequences. Carbon stars with higher mass-loss rates tend to lie along the redder branch, while sources along the blue branch have lower mass-loss rates. We interpret this as evidence of a photospheric C_3 feature that is only visible in the low-mass-loss-rate sources that are relatively unobscured by dusty circumstellar envelopes.

AGB stars are LPVs, so we have examined both the color and the magnitude as a function of period. We find a period-color relationship consistent with the hypothesis of Marengo et al. (2001) that semiregular variables lose mass discontinuously, leading to a lack of hot dust producing redder colors. In contrast, the Mira variables extend along a more linear sequence toward redder colors as we might expect based on the fact that their mass-loss rates are more sustained in time.

The period-luminosity distribution of Galactic AGB

stars is similar to that found by Riebel et al. (2012) for the LMC. Mira variables fall along the fundamental pulsation sequence *C*. Semiregular variables are mostly in sequences *A* and *B*, reflecting the presence of higher overtone modes and shorter periods.

We derive a relationship between mass-loss rate and $[3.6] - [8.0]$ color separately for O-rich AGB stars and carbon stars. The overall shape of the fits is similar to those found by other authors for AGB stars in the LMC, albeit corresponding to a higher mass-loss rate for a given $[3.6] - [8.0]$ color. Discrepancies between our fits and those found by other authors likely reflect different assumptions used in the radiative transfer models used to derive mass-loss rates and uncertainties in the gas-to-dust ratio. In addition, we find that neither color nor mass-loss rate is a good discriminator of chemical type, suggesting that care must be taken when inferring the chemical contribution of dust returned to the ISM by AGB stars.

ACKNOWLEDGEMENTS

We thank the referee, Jacco van Loon, for a thoughtful review and suggestions that improved the quality of the manuscript. This work is based on observations made with the *Spitzer* Space Telescope, which is operated by the Jet Propulsion Laboratory, California Institute of Technology under NASA contract 1407. This research has made use of the SIMBAD database, operated at CDS, Strasbourg, France. Support for this work was provided by NASA through an award issued by JPL/Caltech. This work is also supported by the National Science Foundation's Research Experience for Undergraduates program. MR wishes to thank the REU coordinators Saku Vrtilek, Christine Jones, Melissa Cirtain, and Jonathan McDowell for all their guidance and support.

REFERENCES

- Adelman S.J., Maher D.W., 1998, IBVS, 4591, 1
Aoki W., Tsuji T., Ohnaka K., 1999, IAUS, 191, 175
Baud B., Habing J.H., 1983, A&A, 127, 73
Benjamin R.A. et al., 2003, PASP, 115, 953
Bergeat J., Chevallier L., 2005, A&A, 429, 235
Blanco A., Borghesi A., Fonti S., Orofino V., 2000, A&A, 357, 515
Blum R.D. et al., 2006, AJ, 132, 2034
Boothroyd A.I., Sackmann I.-J., 1992, ApJ, 393, 21
Boyer M.L. et al., 2011, AJ, 142, 103
Boyer M.L. et al., 2012, ApJ, 748, 40
Chen X., Shen Z.-Q., Xu Y., 2007, Chin. J. Astron. Astrophys., 7, 531
Churchwell E. et al., 2009, PASP, 121, 213
Currie T. et al., 2010, ApJS, 186, 191
De Beck E., Decin L., de Koter A., Justtanont K., Verhoelst T., Kemper F., Menten K.M., 2010, A&A, 523, 18
Dupree A.K., Smith G.H., Strader J., 2009, AJ, 138, 1485
Dwek E., Cherchneff I., 2011, ApJ, 727, 63
Fazio G. et al., 2004, ApJS, 154, 10
Feast M.W., Glass I.S., Whitelock P.A., Catchpole R.M., 1989, MNRAS, 241, 375
Ferrarotti A.S., Gail, H.-P., 2006, A&A, 447, 553
Freedman W.L. et al., 2001, ApJ, 553, 47
Gehrz R., 1989, in IAU Symp. 135, Interstellar Dust, ed. L.J. Allamandola & A.G.G.M. Tielens (Cambridge: Cambridge Univ. Press), 445
Gérard E., Le Bertre T., 2006, AJ, 132, 2566
Glass I.S., Schultheis M., Blommaert J.A.D.L., Sahai R., Stute M., Uttenthaler S., 2009, MNRAS, 395, L11
Groenewegen M.A.T., 2006, A&A, 448, 181
Groenewegen M.A.T. et al., 2007, MNRAS, 376, 313
Groenewegen M.A.T., Sloan G.C., Soszyński I., Petersen E.A., 2009, A&A, 506, 1277
Gruendl R.A., Chu Y.-H., Seale J.P., Matsuura M., Speck A.K., Sloan G.C., Looney L.W., 2008, ApJL, 688, 9
Guandalini R. et al., 2006, A&A, 445, 1069
Guandalini R., Busso M., Ciprini S., Silvestro G., Persi P., 2006, A&A, 445, 1069
Guandalini R., Busso M., 2008, A&A, 488, 675
Gullieuszik M. et al., 2012, A&A, 537, 105
Heras A.M., Hony S., 2005, A&A, 439, 171
Humphreys R.M., 1978, ApJS, 38, 309
Humphreys R.M. et al., 1997, AJ, 114, 2778
Hyland A.R., Becklin E.E., Frogel J.A., Neugebauer G., 1972, A&A, 16, 204
Iben I., Jr. 1991, ApJS, 76, 55
Javadi A., van Loon J.Th., Mirtorabi M.T., 2011, MNRAS, 411, 263
Javadi A., van Loon J.Th., Khosroshahi H., Mirtorabi M.T., 2013, MNRAS, 432, 2824
Kerschbaum F., Hron J., 1996, A&A, 308, 486
Knapp G.R., Morris M., 1985, ApJ, 292, 640
Kurayama T., Sasao T., Kobayashi H., 2005, ApJ, 627, 49
Levesque E.M., Massey P., Olsen K.A.G., Plez B., Josselin E., Maeder A., Meynet G., 2005, ApJ, 628, 973
Loup C., Forveille T., Omont A., Paul J.F., 1993, A&AS, 99, 291
Mauas P.J.D., Cacciari C., Pasquini L., 2006, A&A, 454, 609
Marengo M., Busso M., Silvestro G., Persi P., Lagage P.O., 1999, A&A, 348, 501
Marengo M., Ivezić Ž., Knapp G.R., 2001, MNRAS, 324, 1117
Marengo M., Hora J.L., Barmby P., Willner S.P., Allen L.E., Schuster M.T., Fazio G.G., 2007, in proc. “Why Galaxies Care About Stars”, ASP Conf. Series (eds. F. Kerschbaum, C. Charbonnel, R. F. Wing), vol. 378, p. 80 (arXiv:astro-ph/0611346)
Marengo M. et al., 2009, ApJ, 700, 1647
Marshall J.R., van Loon J.Th., Matsuura M., Wood P.R., Zijlstra A.A., Whitelock P.A., 2004, MNRAS, 355, 1348
Massey P., Olsen K.A.G., 2003, AJ, 126, 2867
Matsuura M. et al., 2009, MNRAS, 396, 918
Matsuura M. et al., 2011, Science, 333, 1258
Matsuura M., Woods P.M., Owen P.J., 2013, MNRAS, 429, 2527
Meixner M. et al., 2006, AJ, 132, 2268
Millan-Gabet et al., 2005, ApJ, 620, 961
Monnier J.D. et al., 1997, ApJ, 481, 420
Morris M., Jura M., 1983, ApJ, 267, 179
Nieuwenhuijzen H., De Jager C., 1990, A&A, 231, 134
Noriega-Crespo A., et al., 2004, ApJS, 154, 352

- Olofsson H., González Delgado D., Kerschbaum F., Schöier F.L., 2002, A&A, 391, 1053
- Oudmaijer R.D., Groenewegen M.A.T., Matthews H.E., Blommaert J.A.D.L., Sahu K.C., 1996, MNRAS, 280, 1062
- Ramstedt S., Schöier F.L., Olofsson H., 2009, A&A, 499, 515
- Reimers D., 1975, Man. Soc. Roy. Sci. Liege, Sth Ser., Vol. 8, 369
- Riebel D., Meixner M., Fraser O., Srinivasan S., Cook K., Vijh U., 2010, ApJ, 723, 1195
- Riebel D., Srinivasan S., Sargent B., Meixner M., 2012, ApJ, 753, 71
- Salpeter E.E., 1974, ApJ, 193, 585
- Samus N.N., 2012, General Catalog of Variable Stars (GCVS database, Version 2012Apr)
- Schöier F.L., Ramstedt S., Olofsson H., Lindqvist M., Biegging J.H., Marvel K.B., 2013, A&A, 550, 78
- Schuster M.T., Marengo M., Patten B.M., 2006, Proceedings of the SPIE, 6270-74
- Schuster M.T., 2007, PhD thesis, Univ. Minnesota
- Sedlmayr E. 1994, in Molecules in the Stellar Environment, U.G. Jørgensen (ed.), Springer, Berlin, p.163
- Skrutskie M.T. et al., 2006, AJ, 131, 1163
- Sloan G.C., Price S.D., 1998, ApJS, 119, 141
- Sloan G.C., Kraemer K.E., Price S.D., Shipman R.F. 2003, ApJS, 147, 379
- Smith V.V., Lambert D.L., 1985, ApJ, 294, 326
- Straniero O., Gallino R., Busso M., Chieffi A., Raiteri C.M., Limongi M., Salaris M., 1995, ApJ, 440, 85
- Straniero O., Chieffi A., Limongi M., Busso M., Gallino R., Arlandini C., 1997, ApJ, 478, 332
- Tabur V., Bedding T. R., Kiss L.L., Giles T., Derekas A., Moon T.T., MNRAS, 409, 777
- Tuthill P.G., Monnier J.D., Danchi W.C., Lopez B., 2000, ApJ, 543, 284
- Valentijn E.A. et al., 1996, A&A, 315, 60
- van Belle G.T., Thompson R.R., Creech-Eakman M.J., 2002, AJ, 124, 1706
- van Dyk S., Li W., Filippenko A.V., 2003, PASP, 115, 1289
- van Loon J.Th., Groenewegen M.A.T., de Koter A., Trams N.R., Waters L.B.F.M., Zijlstra A.A., Whitelock P.A., Loup C., 1999, A&A, 351, 559
- van Loon J.Th., 2000, A&A, 354, 125
- van Loon J.Th., Cohen M., Oliveira J.M., Matsuura M., McDonald I., Sloan G.C., Wood P.R., Zijlstra A.A., 2008, A&A, 487, 1055
- van Leeuwen F., 2007, A&A, 474, 653
- Vassiliadis E., Wood P.R., 1993, ApJ, 413, 641
- Ventura P. et al., 2012, MNRAS, 424, 2345
- Verhoelst T., van der Zypen N., Hony S., Decin L., Cami J., Eriksson K., 2009, A&A, 498, 127
- Walker A.R., 2011, Ap&SS, 341, 43
- Werner M. et al., 2004, ApJS, 154, 1
- Whitelock P., Menzies J., Feast M., Marang F., Carter B., Roberts G., Catchpole R., Chapman J., 1994, MNRAS, 267, 711
- Whitelock P.A., Feast M.W., Marang F., Groenewegen M.A.T., 2006, MNRAS, 369, 751
- Whitelock P.A., Feast M.W., van Leeuwen F., 2008, MNRAS, 386, 313
- Wilson O.C., 1976, ApJ, 205, 823
- Willson L.A., 2000, ARA&A, 38, 573
- Wood P.R., Bessell M.S., Fox M.W., 1983, ApJ, 272, 99
- Wood P.R., Whiteoak J.B., Hughes S.M.G., Bessell M.S., Gardner F.F., Hyland A.R., 1992, ApJ, 397, 552
- Wood P.R., 2010, Mem. S. A. It, 81, 883
- Young K., 1995, ApJ, 445, 872
- Zhang B., Reid M.J., Menten K.M., Zheng X.W., Brunthaler A., 2012, A&A, 544, 42
- Zhang K., Jiang B., 2008, ScChG, 51, 1187

Table 1. IRAC AGB OBSERVED TARGETS

Target	IRAS name	Var.	Period [days]	Dist [kpc]	Dist ref.	\dot{M} [M_{\odot}/yr]	\dot{M} ref.	J Mag	H Mag	K Mag
O-RICH STARS										
KU And	00042+4248	M	750	0.68	14	2.4×10^{-5}	11	3.041 ± 0.216	1.829 ± 0.156	1.115 ± 0.208
RW And	00445+3224	M	430	0.86	7	1.9×10^{-7}	17	3.052 ± 0.238	2.225 ± 0.210	1.765 ± 0.228
VY Cas	00484+6238	SRb	100	0.57	16	2.471 ± 0.254	1.484 ± 0.186	1.114 ± 0.234
SV Psc	01438+1850	SRb	102	0.38	12	$3.0 \times 10^{-7} \dagger$	12	2.016 ± 0.244	1.012 ± 0.190	0.722 ± 0.188
RR Per	02251+5102	M	389	0.82	15	3.217 ± 0.244	2.325 ± 0.196	1.662 ± 0.244
RV Cam	04265+5718	SRb	101	0.35	12	2.5×10^{-7}	12	1.667 ± 0.254	0.602 ± 0.164	0.412 ± 0.170
ET Vir	14081-1604	SRb	80	0.14	16	1.651 ± 0.266	0.814 ± 0.290	0.598 ± 0.304
RW Boo	14390+3147	SRb	209	0.29	16	1.560 ± 0.206	0.530 ± 0.150	0.301 ± 0.170
AX Sco	16387-2700	SRb	138	0.34	16	2.159 ± 0.270	1.224 ± 0.282	0.901 ± 0.320
TV Dra	17081+6422	SR	...	0.51	16	2.0×10^{-7}	11	1.942 ± 0.416	1.058 ± 0.174	0.693 ± 0.194
V438 Oph	17123+1107	SRb	169	0.42	4	1.871 ± 0.244	0.935 ± 0.292	0.551 ± 0.312
TY Dra	17361+5746	Lb	...	0.43	12	6.0×10^{-7}	12	2.410 ± 0.296	1.465 ± 0.158	1.083 ± 0.194
CZ Ser	18347-0241	Lb	...	0.44	12	8.0×10^{-7}	12	2.557 ± 0.302	1.405 ± 0.274	0.930 ± 0.310
FI Lyr	18401+2854	SRb	146	0.88	6	3.8×10^{-6}	6	2.040 ± 0.282	1.121 ± 0.164	0.715 ± 0.212
V1351 Cyg	19409+5520	Lb	...	0.32	16	1.816 ± 0.266	0.787 ± 0.170	0.561 ± 0.208
Z Cyg	20000+4954	M	263	0.94	5	4.0×10^{-8}	19	4.176 ± 0.268	3.258 ± 0.228	2.557 ± 0.306
V1300 Aql	20077-0625	M	680	0.66	11	1.3×10^{-5}	11	6.906 ± 0.032	3.923 ± 0.260	2.059 ± 0.262
V584 Aql	20079-0146	Lb	...	0.39	12	5.0×10^{-8}	12	2.136 ± 0.312	1.147 ± 0.204	0.801 ± 0.266
RX Vul	20507+2310	M	457	0.71	18	2.724 ± 0.290	1.655 ± 0.188	1.083 ± 0.228
UX Cyg	20529+3013	M	565	1.85	9	3.2×10^{-6}	11	2.910 ± 0.310	1.887 ± 0.180	1.400 ± 0.194
SS Peg	22315+2418	M	424	0.71	18	2.549 ± 0.270	1.513 ± 0.182	1.121 ± 0.162
V563 Cas	23147+6009	M	534	2.09	11	5.088 ± 0.037	3.882 ± 0.036	3.227 ± 0.248
C-RICH STARS										
VX And	00172+4425	SRa	369	0.56	6	1.4×10^{-7}	6	3.187 ± 0.266	1.891 ± 0.202	1.193 ± 0.202
HV Cas	01080+5327	M	527	0.97	14	3.2×10^{-6}	6	5.585 ± 0.039	3.911 ± 0.222	2.466 ± 0.290
R For	02270-2619	M	339	0.97	14	5.0×10^{-6}	6	4.230 ± 0.274	2.537 ± 0.206	1.349 ± 0.274
V623 Cas	03075+5742	Lb	...	0.51	6	1.1×10^{-7}	6	2.869 ± 0.210	1.706 ± 0.204	1.208 ± 0.212
UV Aur	05185+3227	M	394	1.09	6	1.6×10^{-6}	6	4.029 ± 0.214	3.018 ± 0.192	2.129 ± 0.220
SY Per	04127+4030	SR	474	1.43	6	1.5×10^{-6}	6	4.596 ± 0.316	3.033 ± 0.274	2.132 ± 0.340
TU Tau	05421+2424	SRb	190	1.05	6	5.7×10^{-7}	6	3.331 ± 0.266	2.093 ± 0.210	1.574 ± 0.220
BN Mon	06192+0722	SRb	600	1.28	1	4.2×10^{-6}	6	4.517 ± 0.312	3.096 ± 0.256	2.322 ± 0.308
CR Gem	06315+1606	Lb	...	0.92	6	8.4×10^{-7}	6	3.575 ± 0.302	2.030 ± 0.250	1.538 ± 0.240
V614 Mon	06585-0310	SRb	60	0.48	6	1.5×10^{-8}	6	3.227 ± 0.206	2.307 ± 0.206	1.764 ± 0.224
CGCS 6296	08305-3314	4.21	6	1.3×10^{-4}	6	11.1
SZ Car	09582-5958	SRb	126	0.37	6	4.6×10^{-7}	6	3.206 ± 0.332	2.112 ± 0.280	1.600 ± 0.346
V CrB	15477+3943	M	358	0.84	6	1.3×10^{-6}	6	3.474 ± 0.272	2.209 ± 0.218	1.321 ± 0.276
SX Sco	17441-3541	SR	...	0.83	6	3.8×10^{-7}	6	3.104 ± 0.222	1.884 ± 0.210	1.390 ± 0.254
FX Ser	18040-0941	Lb	...	1.23	6	3.1×10^{-5}	6	7.136 ± 0.023	4.720 ± 0.076	2.702 ± 0.218
DR Ser	18448+0523	Lb	...	1.29	6	1.0×10^{-6}	6	3.833 ± 0.270	2.488 ± 0.218	1.839 ± 0.286
S Sct	18476-0758	SRb	148	0.58	6	5.6×10^{-6}	6	2.303 ± 0.314	1.140 ± 0.262	0.627 ± 0.288
RS Cyg	20115+3834	SRa	418	0.65	6	2.0×10^{-7}	6	3.206 ± 0.228	1.985 ± 0.190	1.321 ± 0.246
T Ind	21168-4514	SRb	320	0.65	6	1.7×10^{-7}	6	1.981 ± 0.248	0.970 ± 0.262	0.564 ± 0.316
S-RICH STARS										
R Gem	07043+2246	M	370	0.71	13	2.1×10^{-6}	11	2.530 ± 0.244	1.642 ± 0.218	1.459 ± 0.226
NQ Pup	07507-1129	Lb	...	0.81	16	3.542 ± 0.292	2.587 ± 0.212	2.306 ± 0.274
S UMa	12417+6121	M	226	1.09	18	4.458 ± 0.214	3.431 ± 0.196	3.017 ± 0.246
R Cyg	19354+5005	M	426	0.44	14	1.6×10^{-7}	11	2.251 ± 0.314	1.379 ± 0.208	0.861 ± 0.246
AA Cyg	20026+3640	SRb	213	0.48	13	2.066 ± 0.288	1.050 ± 0.166	0.625 ± 0.224
X Aqr	22159-2109	M	312	1.32	18	4.710 ± 0.190	3.823 ± 0.196	3.338 ± 0.248
HR Peg	22521+1640	SRb	50	0.42	16	2.306 ± 0.270	1.239 ± 0.194	1.041 ± 0.206
SUPERGIANTS										
XX Per	01597+5459	SRc	415	2.29	3	3.442 ± 0.262	2.480 ± 0.232	1.972 ± 0.242
W Per	02469+5646	SRc	485	2.29	3	3.095 ± 0.202	1.999 ± 0.172	1.568 ± 0.252
NO Aur	05374+3153	Lc	...	0.60	16	2.122 ± 0.322	1.128 ± 0.202	0.971 ± 0.196
U Lac	22456+5453	SRc	...	2.75	10	3.815 ± 0.224	2.672 ± 0.166	1.932 ± 0.206
NML Cyg*	R20445+3955	SRc	940 \ddagger	1.61	20	6.4×10^{-5}	21,22	4.877 ± 0.037	2.389 ± 0.200	0.791 ± 0.204
VX Sgr*	18050-2213	SRc	732	1.57	2	6.1×10^{-5}	4	1.744 ± 0.260	0.550 ± 0.304	-0.122 ± 0.362

* from Table 4.4 in Schuster (2007), \dagger multiple velocity components detected, \ddagger Monnier et al. 1997.**References:** (1) Bergeat & Chevallier 2005; (2) Chen et al. 2007; (3) Currie et al. 2010; (4) De Beck et al. 2010; (5) Feast et al. 1989; (6) Guandalini et al. 2006; (7) Guandalini & Russo 2008; (8) Humphreys 1978; (9) Kurayama et al. 2005; (10) Levesque et al. 2005; (11) Reiter et al. 2014; (12) RAS, MNRAS 000, 1-7.

Table 2. IRAC PHOTOMETRY

Target	IRAS name	epoch	MJD ^a	[3.6]	[4.5]	[5.8]	[8.0]
O-RICH STARS							
KU And	00042+4248	1	53961.9209	1.140±0.031	0.291±0.021	−0.400±0.015	−1.584±0.076
KU And	00042+4248	2	54328.9385	1.747±0.027	0.879±0.024	0.108±0.018	−1.175±0.074
RW And	00445+3224	1	53960.9362	1.109±0.030	1.042±0.028	0.742±0.022	0.216±0.066
RW And	00445+3224	2	54324.8287	0.904±0.025	0.831±0.023	0.546±0.027	0.096±0.059
VY Cas	00484+6238	1	54005.9215	0.879±0.024	0.981±0.027	0.786±0.022	0.564±0.027
VY Cas	00484+6238	2	54149.6210	0.843±0.024	0.929±0.026	0.731±0.032	0.485±0.025
SV Psc	01438+1850	1	53961.9248	0.395±0.023	0.468±0.025	0.256±0.021	−0.027±0.042
SV Psc	01438+1850	2	54149.6256	0.305±0.015	0.411±0.016	0.202±0.020	−0.063±0.031
RR Per	02251+5102	1	54005.9269	0.427±0.024	0.320±0.015	0.044±0.017	−0.289±0.033
RR Per	02251+5102	2	54149.9993	0.764±0.022	0.775±0.022	0.502±0.017	0.202±0.020
RV Cam	04265+5718	1	54005.9347	0.327±0.015	0.451±0.016	0.277±0.021	0.073±0.023
RV Cam	04265+5718	2	54396.8337	0.284±0.014	0.435±0.016	0.216±0.020	0.073±0.023
ET Vir	14081−1604	1	53957.3504	0.395±0.016	0.573±0.018	0.443±0.024	0.372±0.031
ET Vir	14081−1604	2	54148.6245	0.387±0.023	0.537±0.027	0.427±0.024	0.372±0.031
RW Boo	14390+3147	1	53922.4493	0.127±0.018	0.387±0.016	0.145±0.019	−0.053±0.032
RW Boo	14390+3147	2	54149.9923	0.133±0.018	0.387±0.016	0.170±0.019	−0.048±0.033
AX Sco	16387−2700	1	53997.8064	0.564±0.018	0.649±0.020	0.435±0.016	0.256±0.021
AX Sco	16387−2700	2	54357.9155	0.582±0.019	0.700±0.015	0.485±0.017	0.291±0.028
TV Dra	17081+6422	1	54005.9137	0.177±0.021	0.263±0.021	0.061±0.017	−0.123±0.019
TV Dra	17081+6422	2	54286.3724	0.170±0.019	0.242±0.020	0.022±0.017	−0.161±0.019
V438 Oph	17123+1107	1	54002.9634	0.209±0.020	0.294±0.014	0.096±0.018	−0.094±0.020
V438 Oph	17123+1107	2	54357.9197	0.164±0.019	0.263±0.021	0.073±0.017	−0.180±0.020
TY Dra	17361+5746	1	54005.9110	0.679±0.020	0.891±0.020	0.649±0.030	0.284±0.042
TY Dra	17361+5746	2	54286.3697	0.689±0.020	0.879±0.024	0.659±0.030	0.298±0.057
CZ Ser	18347−0241	1	54005.8978	0.519±0.026	0.710±0.021	0.435±0.024	0.277±0.028
CZ Ser	18347−0241	2	54229.6547	0.591±0.037	0.742±0.032	0.476±0.025	0.291±0.028
FI Lyr	18401+2854	1	54005.9018	0.411±0.016	0.601±0.028	0.357±0.023	0.108±0.030
FI Lyr	18401+2854	2	54357.9236	0.419±0.024	0.601±0.019	0.372±0.023	0.114±0.048
V1351 Cyg	19409+5520	1	53956.9174	0.196±0.020	0.395±0.023	0.229±0.020	0.177±0.019
V1351 Cyg	19409+5520	2	54286.3181	0.209±0.020	0.403±0.016	0.222±0.020	0.164±0.025
Z Cyg	20000+4954	1	54005.9076	2.174±0.056	1.892±0.043	1.620±0.047	0.929±0.077
Z Cyg	20000+4954	2	54286.3642	1.862±0.060	1.669±0.051	1.422±0.060	0.753±0.065
V1300 Aql	20077−0625	1	54430.9969	0.145±0.025	−0.483±0.028	−1.187±0.022	−2.280±0.040
V1300 Aql	20077−0625	2	54637.7548	0.649±0.020	0.050±0.017	−0.647±0.024	−1.627±0.036
V584 Aql	20079−0146	1	54064.4277	0.427±0.016	0.502±0.017	0.305±0.022	0.091±0.024
V584 Aql	20079−0146	2	54430.9864	0.427±0.016	0.502±0.017	0.294±0.021	0.033±0.034
RX Vul	20507+2310	1	54286.3354	0.419±0.024	0.468±0.017	0.170±0.019	−0.104±0.020
RX Vul	20507+2310	2	54430.9901	0.493±0.026	0.610±0.029	0.342±0.022	0.044±0.034
UX Cyg	20529+3013	1	54286.3327	1.009±0.027	0.731±0.021	0.411±0.024	−0.403±0.075
UX Cyg	20529+3013	2	54430.9927	1.629±0.034	1.307±0.036	0.968±0.026	0.183±0.051
SS Peg	22315+2418	1	54286.3777	0.820±0.023	0.649±0.020	0.380±0.023	0.005±0.022
SS Peg	22315+2418	2	54100.2776	0.669±0.030	0.669±0.020	0.419±0.016	0.164±0.038
V563 Cas	23147+6009	1	53956.1633	2.585±0.035	2.097±0.037	1.684±0.041	1.036±0.056
V563 Cas	23147+6009	2	54149.4121	2.935±0.032	2.639±0.037	2.190±0.041	1.620±0.097
C-RICH STARS							
VX And	00172+4425	1	53961.0086	0.158±0.019	0.357±0.023	0.485±0.025	−0.216±0.027
VX And	00172+4425	2	54150.6613	0.183±0.019	0.395±0.023	0.528±0.018	−0.157±0.019
HV Cas	01080+5327	1	53961.4766	0.891±0.025	0.342±0.015	−0.108±0.029	−0.589±0.032
HV Cas	01080+5327	2	54150.6238	0.357±0.015	−0.152±0.019	−0.573±0.016	−0.955±0.023
R For	02270−2619	1	53961.0145	−0.476±0.018	−0.900±0.019	−1.227±0.018	−1.621±0.037
R For	02270−2619	2	54357.9070	−0.354±0.016	−0.811±0.016	−1.160±0.019	−1.571±0.051
V623 Cas	03075+5742	1	54005.9318	0.485±0.017	0.546±0.018	0.305±0.022	0.102±0.018
V623 Cas	03075+5742	2	54357.9005	0.493±0.017	0.564±0.018	0.357±0.023	0.120±0.018
SY Per	04127+4030	1	54396.8364	0.820±0.046	0.786±0.034	0.649±0.040	0.605±0.029
SY Per	04127+4030	2	54531.1417	0.942±0.039	0.879±0.037	0.775±0.033	0.387±0.047
UV Aur	05185+3227	1	54005.9383	1.422±0.029	1.017±0.022	0.620±0.019	0.164±0.025
UV Aur	05185+3227	2	54191.1691	1.171±0.026	0.855±0.024	0.451±0.025	0.170±0.025
TU Tau	05421+2424	1	54396.8428	0.981±0.027	1.094±0.029	0.929±0.038	0.411±0.024
TU Tau	05421+2424	2	54188.7098	0.955±0.021	1.051±0.029	0.916±0.025	0.395±0.023
BN Mon	06192+0722	1	54038.7664	1.463±0.029	1.550±0.036	1.422±0.040	1.036±0.042
BN Mon	06192+0722	2	54396.8610	1.454±0.021	1.550±0.032	1.463±0.042	1.022±0.055

Table 2 – *continued*

Target	IRAS name	epoch	MJD ^a	[3.6]	[4.5]	[5.8]	[8.0]
C-RICH STARS							
CR Gem	06315+1606	1	54061.8204	0.995±0.027	0.916±0.025	0.601±0.028	0.485±0.034
CR Gem	06315+1606	2	54396.8582	0.855±0.024	0.867±0.024	0.555±0.027	0.419±0.032
V614 Mon	06585−0310	1	54069.0020	1.272±0.025	1.422±0.028	1.254±0.026	0.955±0.039
V614 Mon	06585−0310	2	54190.6094	1.272±0.025	1.422±0.032	1.265±0.028	1.009±0.041
CGCS 6296	08305−3314	1	54466.0597	4.120±0.048	2.447±0.052	1.124±0.031	−0.133±0.029
CGCS 6296	08305−3314	2	54600.7407	4.674±0.121	2.935±0.049	1.550±0.045	0.183±0.064
SZ Car	09582−5958	1	53888.8675	1.065±0.029	1.171±0.032	1.065±0.029	0.742±0.032
SZ Car	09582−5958	2	54148.6298	0.976±0.027	1.080±0.029	0.916±0.038	0.659±0.030
V CrB	15477+3943	1	53959.8338	0.874±0.019	0.387±0.016	−0.048±0.021	−0.385±0.015
V CrB	15477+3943	2	54152.9619	0.403±0.016	−0.063±0.015	−0.447±0.014	−0.811±0.021
SX Sco	17441−3541	1	53997.2559	0.891±0.049	1.022±0.042	0.942±0.039	0.476±0.034
SX Sco	17441−3541	2	54396.9331	0.867±0.048	1.065±0.043	0.995±0.041	0.476±0.034
FX Ser	18040−0941	1	54002.9673	−0.118±0.019	−0.787±0.016	−1.298±0.023	−1.811±0.041
FX Ser	18040−0941	2	54396.9368	0.263±0.021	−0.433±0.022	−0.969±0.022	−1.505±0.041
DR Ser	18448+0523	1	54039.4356	1.344±0.037	1.505±0.043	1.402±0.040	1.051±0.043
DR Ser	18448+0523	2	54229.1684	1.442±0.041	1.572±0.046	1.505±0.065	1.156±0.063
S Sct	18476−0758	1	54005.8936	−0.058±0.021	0.096±0.024	0.044±0.028	−0.338±0.020
S Sct	18476−0758	2	54396.9396	−0.099±0.020	0.073±0.023	0.028±0.028	−0.385±0.038
RS Cyg	20115+3834	1	54036.9492	0.963±0.026	1.080±0.029	0.867±0.024	0.764±0.055
RS Cyg	20115+3834	2	54286.3299	1.254±0.034	1.065±0.043	0.742±0.022	0.867±0.048
T Ind	21168−4514	1	54069.0284	0.242±0.020	0.380±0.015	0.177±0.019	0.005±0.022
T Ind	21168−4514	2	54430.9820	0.263±0.021	0.387±0.023	0.216±0.020	0.028±0.017
S-RICH STARS							
R Gem	07043+2246	1	54068.8159	1.210±0.027	1.214±0.027	0.891±0.037	0.476±0.051
R Gem	07043+2246	2	54228.7301	1.140±0.031	1.080±0.029	0.786±0.022	0.468±0.033
NQ Pup	07507−1129	1	54069.3910	1.990±0.034	2.190±0.041	2.024±0.065	1.990±0.034
NQ Pup	07507−1129	2	54228.8126	1.990±0.034	2.215±0.042	2.024±0.070	1.990±0.068
S UMa	12417+6121	1	54069.7437	2.620±0.037	2.834±0.030	2.627±0.024	2.468±0.053
S UMa	12417+6121	2	53889.3814	3.002±0.035	3.189±0.041	3.002±0.052	2.798±0.072
R Cyg	19354+5005	1	54005.9052	0.067±0.017	0.022±0.017	−0.377±0.015	−0.856±0.049
R Cyg	19354+5005	2	54286.3666	1.124±0.031	1.009±0.041	0.476±0.034	−0.079±0.051
AA Cyg	20026+3640	1	54065.7245	0.202±0.013	0.528±0.018	0.236±0.020	0.139±0.019
AA Cyg	20026+3640	2	54286.3611	0.216±0.020	0.573±0.018	0.256±0.021	0.177±0.032
X Aqr	22159−2109	1	54286.3244	2.190±0.065	2.135±0.062	1.911±0.044	1.721±0.053
X Aqr	22159−2109	2	54062.9024	2.729±0.047	2.677±0.045	2.447±0.052	2.215±0.042
HR Peg	22521+1640	1	53928.4751	0.649±0.020	0.891±0.025	0.710±0.031	0.620±0.038
HR Peg	22521+1640	2	54095.8618	0.639±0.020	0.843±0.024	0.669±0.030	0.582±0.028
SUPERGIANTS							
XX Per	01597+5459	1	54005.9244	1.171±0.032	1.088±0.030	0.721±0.032	0.085±0.059
XX Per	01597+5459	2	54150.6211	1.220±0.033	1.156±0.032	0.786±0.034	0.145±0.062
W Per	02469+5646	1	54005.9295	1.237±0.036	1.171±0.032	0.808±0.034	0.177±0.064
W Per	02469+5646	2	54152.9557	1.244±0.034	1.178±0.032	0.820±0.035	0.114±0.060
NO Aur	05374+3153	1	54396.8402	0.610±0.019	0.843±0.024	0.582±0.019	0.320±0.029
NO Aur	05374+3153	2	54188.5900	0.620±0.019	0.843±0.024	0.591±0.019	0.312±0.022
U Lac	22456+5453	1	54005.9181	0.786±0.022	0.573±0.018	0.196±0.020	−0.462±0.043
U Lac	22456+5453	2	54328.9353	0.764±0.022	0.564±0.018	0.183±0.019	−0.440±0.024
NML Cyg*	R20445+3955	1	53213.2738	−1.53±0.15	−2.42±0.15	...	−4.53±0.22
VX Sgr*	18050−2213	1	53634.9152	−1.26±0.15	−1.83±0.15	...	−3.36±0.15

^a MDJ = JD−2,400,000.5

* only one epoch; photometry from Schuster (2007, see Table 4.4)

Table 3. Mira/SR P-L sequence

Name	Type	Sequence	Notes
O-RICH STARS			
KU And	M	D	low [3.6], large IR excess – extinction from the circumstellar envelope?
RW And	M	C	along the bottom of the sequence
VY Cas	SRb	$B-C'$	
SV Psc	SRb	C'	
RR Per	M	C	
RV Cam	SRb	C'	
ET Vir	SRb	C	smallest 3.6 μm magnitude
RW Boo	SRb	C	at the bottom of sequence C , small IR excess
AX Sco	SRb	C	near the top of sequence C
V438 Oph	SRb	$C'-C$	
FI Lyr	SRb	B	at the top of sequence B
Z Cyg	M	C	large IR excess
V1300 Aql	M	$C-D$	large IR excess, low 3.6 μm , extinction from the circumstellar envelope?
RX Vul	M	C	large IR excess, lies at the bottom of C
UX Cyg	M	C	one of largest IR excesses
SS Peg	M	$C+$	just below sequence C , modest 3.6 μm and IR excess compared to other Miras of similar period
V563 Cas	M	$C-D$	just below C , among largest IR excesses
C-RICH STARS			
VX And	SRa	C	
HV Cas	M	C	
R For	M	C'	highest Mira 3.6 μm magnitude
UV Aur	M	C	
SY Per	SR	C	
TU Tau	SRb	C'	largest IR excess of the SRs
BN Mon	SRb	$C-D$	falls just below sequence C
V614 Mon	SRb	B	
CGCS 6296	no period available
SZ Car	SRb	C	
V CrB	M	C	
SX Sco	SR	...	no period available
S Sct	SRb	B	
RS Cyg	SRa	$C-D$	one of two SRs below C
T Ind	SRb	C	
S-RICH STARS			
R Gem	M	$C-D$	just below C , modest 3.6 μm and IR excess compared to other Miras of similar period
S UMa	M	C	at the top of sequence C , smallest IR excess of the Miras
R Cyg	M	$C-D$	slightly closer to D than C
AA Cyg	SRb	C	at the top of sequence C
X Aqr	M	C	second smallest Mira IR excess
HR Peg	SRb	A	only source in A
SUPERGIANTS			
XX Per	SRc	C'	SR with large IR excess
W Per	SRc	C'	right along the lower edge of sequence C' ; SR with large IR excess
NML Cyg	SRc	C'	brightest supergiant
VX Sgr	SRc	$B-C'$	along the boundary between sequences B and C' ; second brightest supergiant